Available online at www.sciencedirect.com

ScienceDirect

Geochimica et Cosmochimica Acta 313 (2021) 99–115

Geochimica et Cosmochimica Acta

www.elsevier.com/locate/gca

Rubidium isotope fractionation during chemical weathering of granite

Zhuoying Zhang [a,b,c], Jinlong Ma [a,b,*], Zhibing Wang [a,b], Le Zhang [a,b], Xinyue He [a,b,c], Guanhong Zhu [a,b,c], Ti Zeng [b,d,e], Gangjian Wei [a,b,d]

[a] State Key Laboratory of Isotope Geochemistry, Guangzhou Institute of Geochemistry, Chinese Academy of Sciences, Guangzhou 510640, China
[b] CAS Center for Excellence in Deep Earth Science, Guangzhou 510640, China
[c] College of Earth and Planetary Sciences, University of Chinese Academy of Sciences, Beijing 100049, China
[d] Southern Marine Science and Engineering Guangdong Laboratory, Guangzhou 510640, China
[e] CAS Key Laboratory of Marginal Sea Geology, Guangzhou Institute of Geochemistry, Chinese Academy of Sciences, Guangzhou 510640, China

Received 11 August 2020; accepted in revised form 9 August 2021; available online 19 August 2021

Abstract

Rubidium is an active element on Earth, but whether and how its isotopes fractionate during geological processes are not known yet. In this study, we present data showing large variations in $\delta^{87}Rb$ in bulk samples and individual mineral species from a granite weathering profile in South China as well as in surrounding stream water. The bulk samples show that the mobility of Rb (τRb_{TiO_2}) fluctuates dramatically from −42.0% to 259%, and $\delta^{87}Rb$ values vary from −0.30 ± 0.13‰ in the unaltered bedrock to 0.04 ± 0.08‰ in the weathered saprolites. Significant isotopic variations exist among individual mineral species. In the parent rock, biotite, chlorite, K-feldspar and plagioclase have the $\delta^{87}Rb$ values of −0.42‰, −0.30‰, −0.23‰ and +0.01‰, respectively. In weathered products, major Rb-bearing minerals are K-feldspar, illite and kaolinite. The $\delta^{87}Rb$ values of K-feldspar range from −0.23‰ to 0.14‰, which are likely influenced by the secondary clay minerals adhered on the surface. Illite is the intermediate secondary mineral during biotite and K-feldspar decomposition into kaolinite. The $\delta^{87}Rb$ values of illite vary from −0.28‰ to −0.10‰. As the final product of chemical weathering in this profile, kaolinite has the heaviest isotopic composition, with calculated $\delta^{87}Rb$ values ranging from −0.07‰ to 0.20‰. Chemical weathering drives the $\delta^{87}Rb$ values of saprolites to become heavier. Nearby stream water has the average $\delta^{87}Rb$ value of −0.22‰, which is slightly heavier than the value of parent rock but lighter than the saprolites at the upper part of the profile. Our results demonstrate significant Rb isotope fractionation at the Earth's surface and that adsorption and desorption of clay minerals play a crucial role in triggering Rb isotope fractionation.
© 2021 Elsevier Ltd. All rights reserved.

Keywords: Rubidium; Isotope fractionation; Granite weathering; Adsorption and desorption

1. INTRODUCTION

Rubidium (Rb) is a moderately volatile (Lodders, 2003), lithophile, fluid-mobile (You et al., 1996) element with an atomic number of 37. Because of its high incompatibility (Mckenzie and O'Nions, 1991; Beattie et al., 1993), Rb is enriched in highly differentiated magmatic rocks such as pegmatites. Rb has two isotopes, ^{87}Rb and ^{85}Rb. ^{85}Rb is a stable isotope whereas ^{87}Rb is a radioactive isotope through a β^- decay to ^{87}Sr with a long half-life of 4.976×10^{10} y (Nebel et al., 2011b). Due to the long half-life of ^{87}Rb, we can regard them as stable isotopes in specific geological processes. Thanks to the advancement of

* Corresponding author.
E-mail address: jlma@gig.ac.cn (J. Ma).

https://doi.org/10.1016/j.gca.2021.08.010
0016-7037/© 2021 Elsevier Ltd. All rights reserved.

chemical procedures and precision of mass spectrometry, the reproducibility of $\delta^{87}Rb$ measurements has been improved from 0.2 ~ 0.5‰ (2SD, standard deviation) (Nebel et al., 2005; Nebel et al., 2011a) to 0.06‰ (Pringle and Moynier, 2017; Zhang et al., 2018). Rb isotopes have been demonstrated as a useful proxy for constraining the origin of volatile element variations in the inner solar system (Nebel et al., 2011a; Pringle and Moynier, 2017; Nie and Dauphas, 2019; Zhang et al., 2021b). However, measurements on terrestrial samples are limited and these samples display a very narrow range of $\delta^{87}Rb$ from −0.27‰ to −0.05‰ during magmatic processes (Pringle and Moynier, 2017; Zhang et al., 2018; Nie and Dauphas, 2019). Significant isotope fractionation may occurs in low-temperature processes (Teng et al., 2017), but no investigation of Rb isotopes has been done on these processes yet.

Understanding whether and how Rb isotope fractionation occurs during low-temperature processes has important implications. Continental weathering is a pivotal process linking the atmosphere, hydrosphere, biosphere and lithosphere, which shapes the Earth's topography (Berner and Berner, 2012), influences the ocean chemistry (Opfergelt and Delmelle, 2012), affects the evolution and development of terrestrial ecosystems (Carey et al., 2005) and also regulates the global climate by removing CO_2 from the atmosphere (Raymo et al., 1988; Gaillardet et al., 1999; Dessert et al., 2003; Calmels et al., 2014). Alkali elements show great potential in tracing continental weathering, because of their fluid-mobility, only + 1 valence state, and high abundance in continental crust (Nesbitt et al., 1980). Li and K isotopes are also proven to be powerful tracers for weathering processes (Teng et al., 2010; Misra and Froelich, 2012; Lechler et al., 2015; Santiago et al., 2018; Sun et al., 2018; Li et al., 2019; Chen et al., 2020; Teng et al., 2020). The establishment of a high precision Rb isotope analytical method makes it possible to explore whether Rb isotopes can be a weathering tracer like Li and K isotopes. In addition, Rb behaves slightly different from Li and K during weathering (Nesbitt et al., 1980, Teppen and Miller, 2006). The K/Rb ratio (g/g) is fractionated dramatically during continental weathering, 232 in the crust but 1000 and 3765 in rivers and seawater, respectively (Fabricand et al., 1966; McDonough and Sun, 1995; Wedepohl, 1995; Peltola et al., 2008). The enrichment degree of alkali metal elements in chemical weathering products is often observed as follows: $Cs^+ > Rb^+ > K^+ > Li^+$ (Pauley, 1953; Teppen and Miller, 2006; Zaunbrecher et al., 2015). Whether these differences are also reflected in isotopes is unknown.

Therefore, we investigate Rb isotope fractionation on a well-characterised profile derived from granite weathering in Fogang, Guangdong Province, South China. The variations in Rb concentrations, Rb mobility of weathering products (τRb_{TiO_2}) and Rb isotopic composition ($\delta^{87}Rb$) of the bulk samples in the 40 m-long weathering profile are studied. In addition, individual minerals from seven different bulk samples at different weathering stages, and stream water near the weathering profile are analysed to reveal the distribution of Rb and its isotopes during weathering processes. Our work confirms Rb isotope fractionation during granite chemical weathering and clay minerals have a major control on the fractionation.

2. STUDY AREA AND SAMPLES

The Fogang granite is one of the Early Yanshanian granites in Southeast China (Fig. 1a), which was formed at 160 ± 5 Ma (Li et al., 2009). It is the largest Mesozoic batholith in the Nanling Range with an outcrop of ~6000 km^2 (Fig. 1a) (Li et al., 2009). This region has a warm and humid tropical climate and is influenced by the East Asian monsoon, with mean annual temperature of 25 °C, and annual precipitation ranges from 800 to 2500 mm (mean: 1600 mm) (Wang et al., 2018). High temperatures and abundant precipitation create favourable conditions for chemical weathering.

The studied weathering profile (23°42′28.8″N, 113°30′14.4″E) is located on a small hilltop ~28 m above the surrounding landscape with a gentle slope of 25° (Wang et al., 2018). A stream flows from east to west at the foot of the hill, which is primarily fed by water from the surrounding mountains and merges into the Beijiang River (Fig. 1a). Samples are from a drill core with the top 1.5 m of the soil being discarded. Previous study divided the remaining 40 m-long drill core into four sections, which are, from the bottom, relatively non-weathered parental rock (39.8 m − 31.6 m), slightly weathered granite (31.6 m − 29.3 m), moderately weathered granite (29.3 m − 16.0 m) and highly weathered saprolites and soil (16.0 m − 0.0 m), on the basis of the colour and mineral assemblage (Wang et al., 2018). A simplified section of Fogang granite weathering profile is illustrated in Fig. 1b.

Here, thirty-three bulk samples throughout the weathering profile were selected to reveal the behaviour of Rb and its isotopes during the weathering process (Fig. 1b). Considering significant changes in mineral assemblages during chemical weathering, we also separated individual minerals from seven bulk samples to investigate their Rb concentrations and isotopic ratios. Six water samples from the stream at the foot of the hill over different months were collected to explore the relationship of Rb isotopic composition between the stream water and the weathered saprolites.

3. ANALYTICAL METHODS

All laboratory work was carried out at the State Key Laboratory of Isotope Geochemistry, Guangzhou Institute of Geochemistry, Chinese Academy of Sciences (GIGCAS). Wang et al. (2018) reported pH values, mineral contents, major and trace elements of some samples from this profile, and the data of new samples were obtained following the methods described by Wang et al. (2018). The pH values of the weathering products were measured by a Thermo Orion Star A (520M-01A), mineral composition was analysed by a Bruker D8 Advance X-ray diffractometer (XRD), and major and trace elements were measured by a Rigaku ZSX100e X-ray fluorescence spectrometer (XRF) and Thermo Element inductively coupled plasma mass spectrometer (ICP-MS). In situ trace element measurements of minerals were conducted using a Thermo

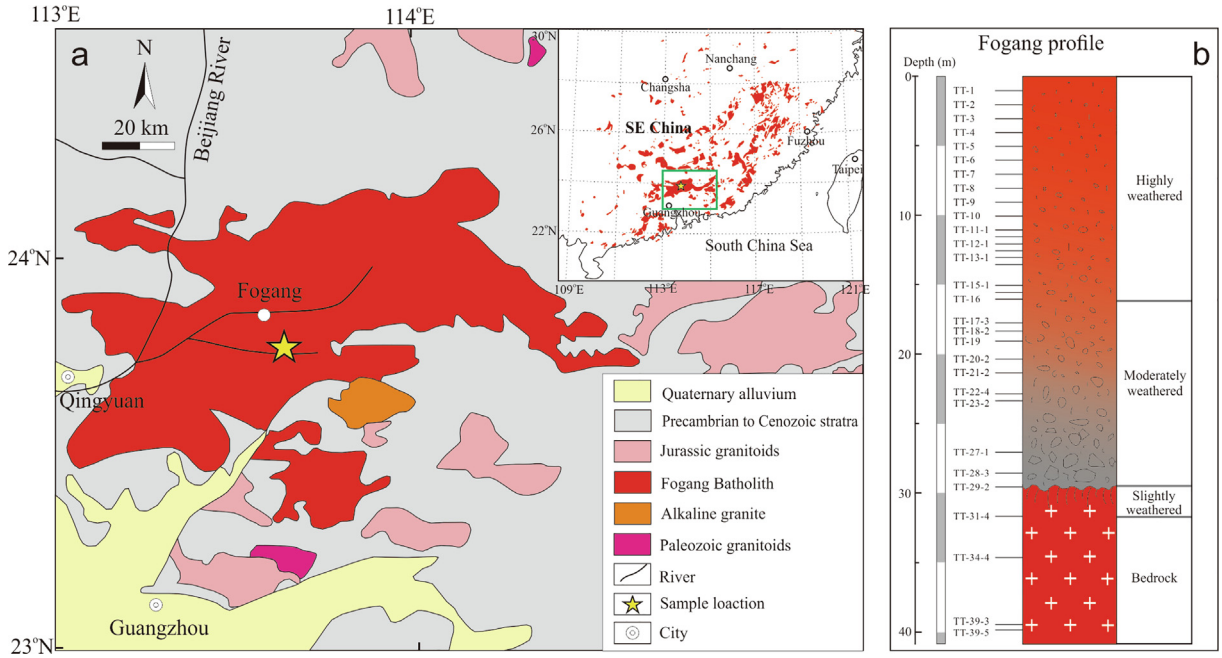

Fig. 1. (a) Simplified geological map of the study area in Fogang County. Sampling location is donated by yellow star. Inset showing the distribution of Mesozoic granites (After Li et al., 2009); (b) Simplified section of Fogang granite weathering profile which is divided into four stages based on colour and texture (after Wang et al. 2018). Horizontal lines indicate the sampling locations.

Fisher Scientific inductively coupled plasma-sector field-mass spectrometry (ICP-SF-MS) coupled with a 193-nm (ArF) Resonetics RESOlution M-50 laser ablation system, following the method described by Zhang et al. (2019). The Rb isotopic analysis includes sample preparation, chemical purification and instrumental measurement, which are shown with details below.

3.1. Sample preparation

Individual mineral species, including K-feldspar, plagioclase, biotite, chlorite and illite were picked from the bulk samples after cleaning, crushing, sieving, and panning. Each type of mineral was cleaned with Milli-Q water before ground into powder.

Approximately 10–30 mg powder of the bulk and mineral samples were digested in an acid mixture of HF–HNO_3 for 7 days in capped beakers on a hot plate at a temperature of 120 °C. After complete evaporation, 1 mL of aqua regia was added in the capped beakers for an additional 4 hours dissolution, to ensure all samples dissolved entirely. Then all the samples were evaporated to dryness, 1 mL of concentrated HNO_3 were added into the beakers, dried again, and repeated these steps twice. After that, 2 mL of 1:1 HNO_3 was added and heating at 120 °C for 4 hours. The samples were dried, re-dissolved with 2.7 M HNO_3, and heated in the capped beakers for 4 hours for chemical purification (Zhang et al., 2018).

Six stream water samples were filtered through 0.45 μm Millipore membrane filters and acidified to pH < 2 using distilled nitric acid in the field immediately. All the samples were collected in 500 mL pre-cleaned PP bottles. 4 mL of each stream water was taken to measure major and trace elements by ICP-AES and ICP-MS, respectively. According to the Rb content of each water sample, approximately 20–30 mL of water samples were evaporated to dryness in beakers on a hot plate at a temperature of 120 °C. In order to avoid interference from organic matter, 0.5 mL of concentrated H_2O_2 was added to each sample during the evaporation process. Then 1 mL of concentrated HNO_3 were added into the beakers and dried again, repeating this step twice. After that, each sample were dissolved with 2 mL of 1:1 HNO_3 in the capped beakers on a hot plate for 4 hours. Finally, they were dried again and dissolved with 0.15 mL of 2.7 M HNO_3 in the capped beakers on a hot plate for 4 hours for chemical purification.

3.2. Column chemistry

Quartz column with a diameter of 0.4 cm and a length of 20 cm, filled with 2.5 mL of Sr-spec resin (50–100 mesh) was used to separate Rb from matrix elements. Resin was firstly washed and conditioned following the description by Zhang et al. (2018). Then, 0.1 mL of the dissolved sample material was loaded onto the pre-cleaned resin, followed by addition of 3 mL of 2.7 M HNO_3 which can remove most matrix elements (especially Na, Mg, Al, and Ca). After that, Rb was collected with 4 mL of 2.7 M HNO_3 before K was washed out of the column. Only small amount of Na (<0.20 wt. % of total Na) and Ca (<0.40 wt. % of total Ca) had been detected in the 4 mL of Rb eluted solutions. According to our previous test that when Na/Rb weight ratio is less than 2 and Ca/Rb weight ratio is less than 4, the purified solution can meet the requirements for high-precision measurement (Zhang et al., 2018). Because most samples in this study are granite,

aluminosilicate minerals with relatively high Rb but low Na, Ca contents, and stream water samples with low Rb content but low Na, Ca contents, one column purification is enough. Only the plagioclase which has low Rb but high Na and Ca contents was purified by Sr-Spec resin for twice to remove residual Na and Ca. We collected 200 μL of washing solution before and after Rb eluted solutions, respectively, and took 100 μL sample out of the 4 mL of Rb purification solution for ICP-MS measurement, to ensure the recovery of Rb close to 100% and the residual matrix not affecting high-precision measurement of Rb isotopes by MC-ICP-MS. Finally, the eluted solutions were dried and re-dissolved in 2% HNO_3 for Rb isotope measurement.

3.3. Instrument measurement

The Rb isotope analysis was carried out using a Thermo Fisher Scientific Neptune Plus multi-collector inductively coupled plasma mass spectrometry (MC-ICP-MS). Sample solutions were introduced through a PFA nebulizer (~50 μL min^{-1}, ESI) and a quartz dual cyclonic-Scott spray chamber (Thermo Fisher Scientific). An X skimmer cone was used at the interface to improve the sensitivity of the instrument. The signals of ^{85}Rb, ^{87}Rb and ^{88}Sr were detected by the L2, the axial and the H1 Faraday cups, respectively. The isobaric interference of ^{87}Sr on ^{87}Rb was corrected by monitoring the signals of ^{88}Sr (generally less than 1 mV) by $^{87}Sr = 0.085 \times {}^{88}Sr$. Sample-standard bracketing (SSB) mode was used for mass bias corrections and NIST SRM 984 was selected as the calibrator. The $\delta^{87}Rb$ of the samples was calculated as the equation shown below:

$$\delta^{87}Rb‰ = \left(\frac{2 \times {}^{87}Rb/{}^{85}Rb_{sample}}{{}^{87}Rb/{}^{85}Rb_{NISTSRM984A} + {}^{87}Rb/{}^{85}Rb_{NISTSRM984B}} - 1 \right) \times 1000 \quad (1)$$

where NIST SRM 984A and NIST SRM 984B serves as the calibrator measured after and before the sample, respectively. Both the sample and the standard solution were diluted with 2% HNO_3 and their concentrations were adjusted to 100 ng mL^{-1}, which yielded a ^{85}Rb isotopic intensity about 5 V, to reduce the difference of mass bias between the sample and the NIST SRM 984 standard solution during Rb isotope measurement. After each Rb isotope measurement, the signal of ^{85}Rb decreased to within 1 mV after 5 min of washing with 2% HNO_3. The signal-to-background ratio for each measurement can be better than 5000, so the influence of the background on Rb isotope measurement could be regarded as negligible. The procedural Rb blanks for the bulk samples and minerals were generally lower than 1 ng, far less than the total Rb in the samples (300–2700 ng); thus, the influence of the blank could be ignored during the analytical procedure.

The NIST SRM 984 standard solution and three standard samples (JG-2, AGV-2 and W-2a) that were chemically treated with the samples were repeatedly measured accompanying with the samples. The $\delta^{87}Rb$ results of these standards are 0.00 ± 0.06‰ (2SD, N = 261) for NIST SRM 984, −0.20 ± 0.06‰ (2SD, N = 14) for JG-2, −0.08 ± 0.04‰ (2SD, N = 6) for AGV-2 and −0.11 ± 0.02‰ (2SD, N = 7) for W-2a. The results coincide with previously published values within analytical error (Pringle and Moynier, 2017; Zhang et al., 2018).

4. RESULTS

The Rb concentrations of bulk samples are presented in Table 1, which show an upward increase trend from 311 μg/g of the bedrock to 724 μg/g at 15.5 m, then decreases to the minimal (177 μg/g) at 1 m. To quantitatively evaluate the relative depletion or enrichment of an element during chemical weathering, the mobility of elements in weathering products is calculated into the τ value, defined as follows (Nesbitt, 1979):

$$\tau E(\%)_I = \left[(E/I)_s - ((E/I)_p) \right] / (E/I)_p \times 100 \quad (2)$$

where E is the target element, I is the relatively immobile constituent, and s and p indicate saprolite (weathering product) and parent rock, respectively. Here, we choose Ti as an immobile agent because TiO_2 concentration is high and generally conservative during chemical weathering (Nesbitt, 1979). The unaltered bedrock accounts for approximately 8 m (from 39.8 m to 31.6 m) in this profile (Wang et al., 2018), and the values of the studied elements in unaltered rocks are calculated by averaging the samples from TT-32-2 to TT-39-5 to better reflect the overall characteristics of the bedrock. The τ values of Rb and K relative to TiO_2 in the Fogang granite weathering profile are presented in Table 1. From 29.3 m to 6.0 m, the τRb_{TiO_2} increases from −5.05% to 259%, suggesting that the section undergoes Rb enrichment. From 6.0 m to the top of the profile, τRb_{TiO_2} decreases from 55.0% to −42.0%, showing that the enrichment degree of Rb is gradually weakened. The saprolites near the surface even exhibit a Rb loss trend (Table 1 and Fig. 2).

The $\delta^{87}Rb$ values of the bulk samples in the whole profile range from −0.30‰ to 0.04‰. The values in the unaltered parent rocks are relatively uniform with a mean $\delta^{87}Rb$ of −0.26 ± 0.09‰, which are close to the value of previously measured granite standard G-2, −0.27 ± 0.06‰ (Zhang et al., 2018). The heaviest $\delta^{87}Rb$ values occur at ~6.0 m of 0.04‰. Measurable fractionations are observed in the profile, and $\delta^{87}Rb$ values show a tendency to become heavier with increasing chemical weathering intensity (Table 1 and Fig. 2).

The mineral contents data of Fogang granite weathering profile are listed in Table 2 and exhibited by Fig. 3. The bottom bedrock (39.8 m − 31.6 m) is dominated by quartz, K-feldspar, plagioclase, biotite, and chlorite. Biotite and chlorite disappear at ~ 31.6 m and plagioclase decomposed completely at ~27.3 m. Kaolinite and illite form above 29.5 m and gradually increase with depth decrease. With the enhancement of chemical weathering, quartz, K-feldspar and clay minerals become the dominant minerals. Rb concentrations and $\delta^{87}Rb$ of individual mineral species from seven different depths are listed in Table 3 and shown in Fig. 4. Rb concentrations of each mineral

Table 1
Rb concentrations and isotope compositions of the bulk samples with the variations in depth, τRb_{TiO_2}, $\tau K_2O_{TiO_2}$, CIA, pH and TOC.

Sample	Depth (m)	τRb_{TiO_2}(%)	$\tau K_2O_{TiO_2}$(%)	CIA[a] (%)	pH	TOC (%)	Rb (μg/g)	$\delta^{87}Rb$ (‰)	2SD	n
TT-1	1.0	−42.0	−68.2	89.6	5.06		177	−0.15	0.03	4
TT-2	2.0	−5.45	−28.1	78.7*	4.88*	0.10*	265	−0.11	0.04	3
TT-3	3.0	5.89	−15.0	74.6	4.99		257	−0.14	0.11	4
TT-4	4.0	43.0	13.0	63.3	5.42		392	−0.17	0.12	5
TT-5	5.0	55.0	−2.89	64.3	5.31		442	−0.21	0.07	4
TT-6	6.0	259	143	70.4*	5.15*	0.07*	396	0.04	0.08	3
TT-7	7.0	89.2	34.6	63.7	6.14		280	−0.12	0.10	5
TT-8	8.0	216	134	70.8	6.24		394	−0.11	0.05	4
TT-9	9.0	246	164	66.1	6.02		440	−0.02	0.13	4
TT-10	10.0	222	140	68.0*	5.63*	0.13*	496	−0.15	0.06	3
TT-11-1	11.0	166	103	63.3			450	−0.11	0.10	6
TT-11-2	11.5	149	82.0	65.9			506	−0.09	0.09	4
TT-12-1	12.0	187	137	65.2			521	−0.07	0.07	4
TT-12-2	12.5	191	136	64.5*	5.25*	0.05*	532	−0.11	0.06	4
TT-13-1	13.0	85.3	17.0	76.8			346	−0.11	0.12	4
TT-13-2	13.5	150	101	70.1			374	−0.09	0.12	9
TT-15-1	15.0	83.6	30.3	63.9			613	−0.26	0.10	7
TT-15-2	15.5	67.4	−15.5	67.3	5.34	0.05	724	−0.27	0.12	5
TT-16	16.0	117	75.4	60.3*	5.82*	0.05*	550	−0.22	0.02	5
TT-17-3	17.7	144	43.8	62.8*	5.63*	0.05*	575	−0.02	0.06	6
TT-18-2	18.3	31.9	3.79	65.2*	5.82*	0.07*	450	−0.13	0.07	4
TT-19	19.0	126	113	61.1*	5.86*	0.06*	438	−0.23	0.09	4
TT-20-2	20.3	45.3	37.4	66.6*	6.06*	0.06*	414	−0.11	0.04	4
TT-21-2	21.3	27.4	14.8	66.1*	6.16*	0.05*	417	−0.17	0.02	4
TT-22-4	22.8	14.8	22.1	61.5*	6.22*	0.06*	402	−0.21	0.04	4
TT-23-2	23.3	29.1	23.4	61.2*	6.87*	0.05*	412	−0.16	0.07	4
TT-27-1	27.0	51.4	60.2	56.8*	6.83*	0.05*	379	−0.28	0.10	5
TT-28-3	28.5	34.5	28.4	60.6*	7.03*	0.06*	398	−0.16	0.06	2
TT-29-2	29.5	−5.05	−12.9	63.4*	6.93*	0.06*	355	−0.13	0.05	4
TT-31-4	31.6	63.9	44.6	52.6*	8.74*	0.07*	323	−0.26	0.04	2
TT-34-4	34.6	10.6	21.9	50.8*	9.74*	0.06*	344	−0.28	0.11	5
TT-39-3	39.4	3.48	13.1	48.1*	9.46*	0.06*	311	−0.30	0.13	4
TT-39-5	39.8	−25.7	−32.4	49.8*	9.50*	0.08*	321	−0.20	0.03	3

a: Chemical index of alteration (CIA) is defined as molar Al_2O_3 / (Al_2O_3 + CaO + Na_2O + K_2O) × 100 (Nesbitt and Young, 1982). The major elements used for calculation are listed in Table B as supplementary data.
*: Data with asterisk are from Wang et al. (2018).

species change significantly except for quartz and plagioclase, which contain neglectable Rb. The main Rb-bearing minerals in TT-39–5 are biotite, K-feldspar and chlorite, which have Rb content of 1160 μg/g, 563 μg/g and 363 μg/g, respectively. In weathered residues, the main Rb-bearing minerals become K-feldspar and illite, which contain 563 μg/g ~ 1031 μg/g and 191 μg/g ~ 984 μg/g of Rb, respectively (Fig. 4a). The $\delta^{87}Rb$ values of each mineral species also vary with depths. $\delta^{87}Rb$ of K-feldspar change from −0.23‰ in TT-39–5 to 0.06‰ in TT-2. The $\delta^{87}Rb$ values of illite become lighter from −0.10‰ in TT-28–3 to −0.28‰ in TT-10, then rise to −0.19‰ in TT-2 (Fig. 4b). Kaolinite in these samples appears as crypto-crystals, and they cannot be isolated for Rb content and isotope analysis.

Six stream waters collected near the weathering profile contain low Rb content (10.06 ng/g to 18.9 ng/g) but display a large range in $\delta^{87}Rb$ (from − 0.40‰ to −0.10‰), with an average of −0.22 ± 0.10‰ (Table 4 and Fig. 5).

5. DISCUSSION

Rb isotopes are significantly fractionated within the Fogang granite profile with low $\delta^{87}Rb$ (mean: −0.26 ± 0.09‰) in relatively non-weathered rocks and variable but generally high $\delta^{87}Rb$ (-0.30‰ to 0.04‰) in weathered residues (Table 1 and Fig. 2). The positive correlations between τRb_{TiO_2}, CIA and $\delta^{87}Rb$ (Fig. 6a and b) strongly support chemical weathering resulting in Rb migration and Rb isotope fractionation. Exogenous input (such as aeolian dust and rainwater) and internal processes during chemical weathering (such as decomposition of primary minerals, formation of secondary minerals, changes in pH, and biological activity) may cause variations of the Rb concentrations and $\delta^{87}Rb$ in the weathering products. To better understand the behaviour of Rb and its isotopes during chemical weathering process, these factors are evaluated below.

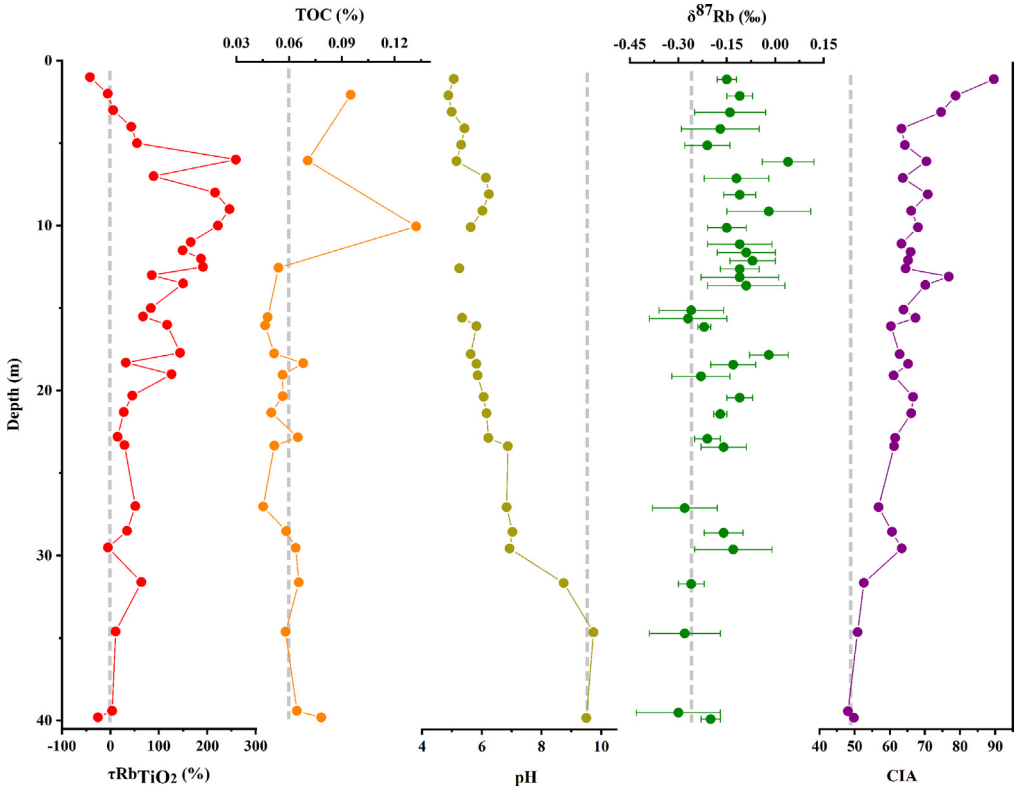

Fig. 2. Variations in τRb_{TiO_2}, TOC, pH, $\delta^{87}Rb$ and CIA with depth in the granite weathering profile. Error bars represent 2 standard deviation (2SD).

5.1. The influence of exogenous input and biological activity

External inputs mainly include precipitation and aeolian dust. Precipitation is one of the important extraneous sources that influence the isotopic ratios in the upper sections of weathering profiles (Ma et al., 2010; Lara et al., 2014; Siebert et al., 2015; Wang et al., 2020). Available data show very low Rb concentration in rainfall between 0.2 and 1.5 ng/g (Stössel and Prange, 1985; Berg et al., 1994; Shimamura et al., 2007). Given the hundreds of μg/g level of Rb in each weathered sample, the effect of short-term rainfall on the Rb content and isotopic composition of the profile should be negligible. The effect of long-term accumulation of rainwater on Rb isotopic composition of the weathering profile is evaluated by following calculation:

$$Rb_{rainwater} = \frac{C^{Rb}_{rainwater} \times MAP \times s \times t}{\rho \times H \times s} \quad (3)$$

where $C^{Rb}_{rainwater}$ is the Rb concentration of precipitation, MAP is the Mean Annual Precipitation, s is unit area (1 m^2), t is the weathering age of entire weathering profile, ρ is the density of granite weathering crust (1.5 g/cm^3) (Pistiner and Henderson, 2003), H is the height of the weathering profile (33.1 m). Average Rb concentration in rainfall of 0.85 ng/g (Stössel and Prange, 1985; Berg et al., 1994; Shimamura et al., 2007) and MAP of 1650 mm (Wang et al. 2018) are used here. Weathering age t is calculated by:

$$t = H/v \quad (4)$$

where v is the granite erosion rates of about 20 m/Ma (Kuhlemann et al., 2007; Mahara et al., 2010; Cui et al., 2014; Cui et al., 2016). According to equation (3) and equation (4), the accumulated Rb content of rainwater on the granite profile since chemical weathering is about 46.8 μg/g. The mean content of Rb in bulk samples throughout the profile is 427 μg/g and Rb content in weathered residues reaches 724 μg/g. Even if all the Rb in rainwater becomes concentrated in the profile, the accumulated Rb content from rainwater is generally less than 10% of the whole rock. Furthermore, the main Rb-bearing phases in the profile are K-feldspar (primary mineral), illite and kaolinite (secondary minerals). Of these, K-feldspar has high Rb content (Table 3) and contributes the major Rb to the weathered section. The Rb^+ in rainwater can be concentrated in the profile through adsorption by illite or kaolinite. The greater influence should occur in the top section where more secondary minerals are formed (Table 2). However, this is not observed in the studied profile. In addition, in order to minimize the influence of rainwater, the top 1.5 m of the soil has been discarded. Thus, rainwater input for Rb should has neglectable influence in this profile.

For aeolian dust, we think the influence of loess is very limited based on the following arguments: (1) The deposition of loess mainly influences the Rb content and the value of $\delta^{87}Rb$ at the top of the profile. In order to eliminate the

Table 2
Mineral proportions in samples from Fogang granite weathering profile.

Sample	Depth (m)	Quartz (wt. %)	K-feldspar (wt. %)	Plagioclase (wt. %)	Biotite (wt. %)	Chlorite (wt. %)	Illite (wt. %)	Kaolinite (wt. %)
TT-1	1.0	31.8	4.20				4.20	57.0
TT-2*	2.0	24.8	20.0				9.30	43.6
TT-3	3.0	29.1	18.1				12.1	40.7
TT-4	4.0	27.0	23.7				12.4	35.7
TT-5	5.0	36.2	21.7				12.5	29.6
TT-6*	6.0	39.9	16.4				9.50	34.2
TT-7	7.0	40.5	14.2				7.50	37.8
TT-8	8.0	32.8	13.0				14.3	39.8
TT-9	9.0	35.1	17.7				14.1	33.1
TT-10*	10.0	31.6	39.1				3.50	25.7
TT-11-1	11.0	28.3	27.8				6.40	37.5
TT-11-2	11.5	37.0	34.9					28.1
TT-12-1	12.0	31.5	44.9					23.7
TT-12-2*	12.5	21.3	49.9				7.90	21.0
TT-13-1	13.0	34.1	13.4				12.2	40.3
TT-13-2	13.5	37.3	29.1					33.6
TT-15-1	15.0	28.5	43.2					28.3
TT-15-2	15.5	15.0	16.5				11.6	39.1
TT-16*	16.0	20.7	41.9				7.30	20.9
TT-17-3*	17.7	29.0	27.5				12.5	31.0
TT-18-2*	18.3	27.3	24.4				15.4	32.9
TT-19*	19.0	25.5	37.7				17.8	19.0
TT-20-2*	20.3	17.7	56.6				8.60	17.1
TT-21-2*	21.3	20.5	29.3				20.7	29.5
TT-22-4*	22.8	17.3	38.9				12.8	20.4
TT-23-2*	23.3	41.3	27.0				16.1	15.5
TT-27-1*	27.0	27.0	43.7	9.50			9.90	10.0
TT-28-3*	28.5	20.6	54.7	8.10			5.40	11.3
TT-29-2*	29.5	23.1	38.3	15.8			8.40	7.70
TT-31-4*	31.6	36.1	27.6	32.9		3.40		
TT-34-4*	34.6	26.2	37.9	25.0	7.10	3.50		
TT-39-3*	39.4	25.7	23.8	33.9	11.4	5.20		
TT-39-5*	39.8	23.5	24.0	32.4	9.80	10.4		

*: Data with asterisk are from Wang et al. (2018).

interference of loess, the ~1.5 m topsoil had been discarded at the beginning of drilling the 40 m-long rock core. (2) The loess (Taylor et al., 1983) and Fogang weathered samples plotted in two different groups in the La–Th–Sc discrimination diagram (Wang et al., 2018), indicating the limited influence of loess on this profile.

Little is known about the Rb uptake by plants from soil. To minimize biological influence, the ~1.5 m soil at the top of the profile was removed. In addition, the total organic carbon (TOC) content in the whole profile is very low, varying from 0.05% to 0.13% (Table 1), indicating that the influence of biological activities is limited.

5.2. Rb concentrations and δ^{87}Rb variations controlled by minerals

Releasing cations during incongruent weathering of primary minerals, and adsorption and desorption of the same cations onto the secondary clay minerals are important processes resulting in element migration (Nesbitt et al., 1980), and fractionations of Li, K and Mg isotopes during these processes have been extensively reported (Huang et al., 2012; Tsai et al., 2014; Teng et al., 2020). Rb isotopic compositions of bulk samples (except for the top one) in Fogang weathering profile show a positive correlation with CIA (Fig. 6b) and (Illite + Kaolinite)/K-feldspar ratio (Fig. 6d), indicating that the Rb isotopic composition is associated with minerals. To identify these mineralogical processes, individual minerals separate from different depths throughout the whole profile are investigated. Given the low Rb contents in quartz and plagioclase (<2 μg/g, Table 3), which have little contribution to the bulk δ^{87}Rb, the analyses are mostly done on available Rb-rich minerals. Each mineral species shows large Rb concentration and isotopic variations in different depths which may be caused by mineral heterogeneity or mineralogical processes during weathering.

5.2.1. *Influence of mineral heterogeneity*

In-situ analyses show that K-feldspar grains separated from the same bulk sample have a large range of Rb contents, and obvious variation also occurs within a single grain (Fig. 7 and Table A), confirming the Rb content heterogeneity within mineral. In order to assess the Rb iso-

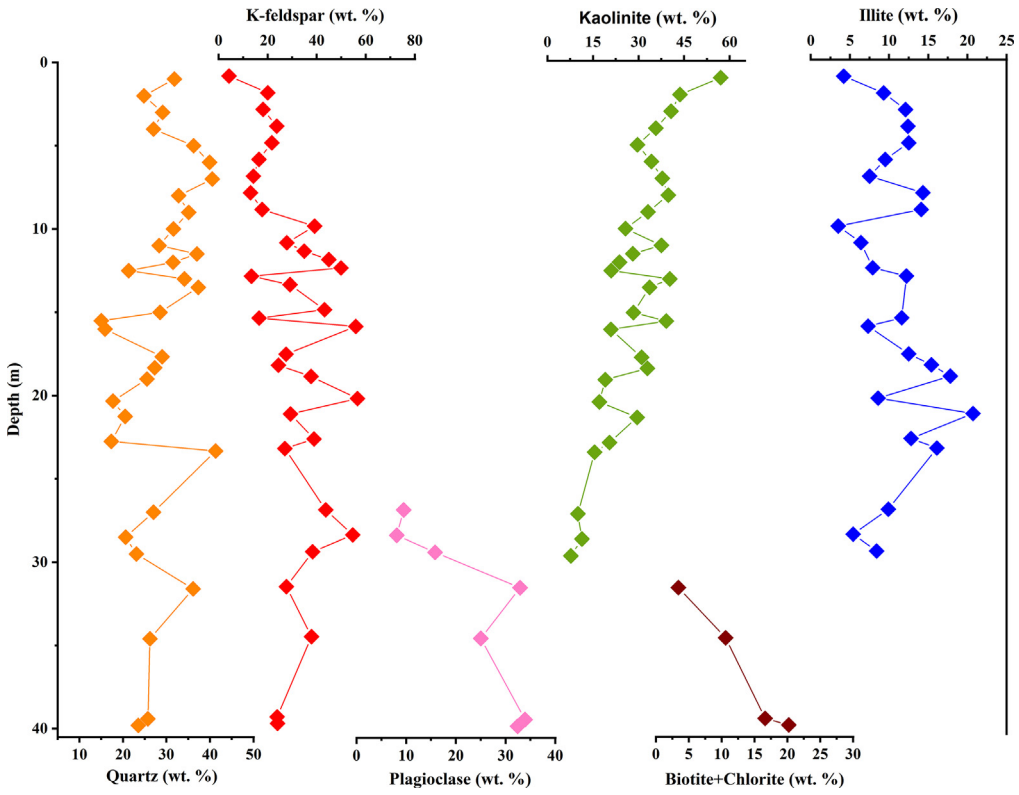

Fig. 3. Variations in mineral proportion (wt. %) with depth, including quartz, K-feldspar, plagioclase, biotite, chlorite, illite and kaolinite in the Fogang granite weathering profile.

topic heterogeneity among a certain mineral species from the same sample, about 40 mg of K-feldspar, biotite and plagioclase grains are randomly selected from TT-10, TT-35-5 and TT-39-3, respectively. Each mineral species is divided into two different portions for grinding into powders then for isotopic determination. The δ^{87}Rb value of the same mineral from the same sample only show tiny difference (0.01‰ ~ 0.03‰), except for the two portions of K-feldspar from TT-35-5 that show 0.07‰ variation (Table 5). Considering that the long-term precision of the instrument is about 0.06‰, we deem that the influence of mineral heterogeneity is small. Approximately 0.4‰ fractionation is found among different minerals in the fresh parent rock. Larger differences display in the same mineral species from different depths (e.g., δ^{87}Rb values of K-feldspar vary from −0.23‰ to +0.14‰, and δ^{87}Rb values of illite range from −0.28‰ to −0.10‰); therefore, we believe that mineralogical processes have larger influence on the isotopic variation than mineral heterogeneity.

5.2.2. Rb isotopic composition of individual minerals in parent rock

The parent rock sample (TT-39-5) consists of biotite (9.8 wt. %), plagioclase (32.4 wt. %), quartz (23.5 wt. %), K-feldspar (24.0 wt. %) and secondary chlorite (10 wt. %). The Rb content and δ^{87}Rb value of bulk sample and individual minerals are shown in Fig. 4 and Table 3. Rb-bearing minerals are biotite, chlorite and K-feldspar, showing lighter δ^{87}Rb value than bulk sample. Plagioclase has 2.4 μg/g Rb content and heaviest δ^{87}Rb value. The chlorite, an alteration of biotite, has higher δ^{87}Rb than biotite, indicating incongruent degradation of biotite leaving heavy δ^{87}Rb in the residues. It's worth noting that TT-39-5 bulk sample has higher δ^{87}Rb value (-0.20‰) than all Rb-rich minerals separated from this sample, but other parental rocks have obvious lower and narrow δ^{87}Rb between −0.26‰ to −0.30‰, which may reflect the influence of mineral heterogeneity (uncertainty from the individual minerals, which is less than 0.07‰) or the long-term precision of the instrument (uncertainty from the bulk sample which is about 0.06‰) or the uncertainties in XRD mineral analysis (~5%).

Nevertheless, the 0.43‰ variation of δ^{87}Rb among individual minerals is significantly larger than the measurement uncertainty (0.06‰), which may be caused by: (1) equilibrium fractionation between silicate melt and crystalline minerals; (2) kinetic processes. Theoretical calculation suggested that equilibrium fractionation can only cause less than 0.01‰ variations between silicate melt and crystal minerals under 1100 ° C ~ 900℃ (Zeng et al., 2019). Therefore, the Rb isotope fractionation between individual minerals is more likely to be associated with kinetic processes. This raises the question of whether Rb isotopes fractionate during kinetic processes, such as fractional crystallization, metamorphism, and diffusion. To clarify these processes is beyond the scope of this study.

Table 3
Rb concentrations and δ^{87}Rb values of bulk samples and separated minerals from Fogang granite weathering profile.

Sample ID	Sample type	Mineral content (wt. %)	Rb content (μg/g)	Rb contribution (%)	Rb contribution of unpicked minerals (%)	δ^{87}Rb (‰)	2SD	n	Calculated Rb content of kaolinite (μg/g)	Calculated δ^{87}Rb of kaolinite (‰)
TT-2	Bulk sample		269		34.37	−0.11	0.04	3		
	K-feldspar	20.0	794	59.03		0.07	0.06	3		
	Illite	9.30	191	6.60		−0.19	0.02	4		
	Kaolinite	43.6							318	0.12
TT-6	Bulk sample		396		63.93	0.04	0.08	3		
	K-feldspar	16.4	1031	23.30		−0.08	0.08	12		
	Illite	9.50	532	12.77		−0.24	0.10	6		
	Kaolinite	34.2							740	0.20
TT-10	Bulk sample		504		51.00	−0.15	0.06	3		
	K-feldspar	39.1	924	43.65		−0.16	0.06	8		
	Illite	3.50	771	5.35		−0.28	0.05	5		
	Kaolinite	25.7							1000	−0.07
TT-20-2	Bulk sample		414		2.52	−0.11	0.04	4		
	K-feldspar	56.6	637	87.14		−0.14	0.05	4		
	Illite	8.60	498	10.34		−0.17	0.05	2		
	Kaolinite	17.1								
TT-23-2	Bulk sample		436		28.83	−0.16	0.07	4		
	K-feldspar	27.0	744	34.83		−0.13	0.05	5		
	Illite	16.1	984	36.34		−0.20	0.08	3		
	Kaolinite	15.5							811	−0.01
TT-28-3	Bulk sample		398		7.44	−0.16	0.06	2		
	K-feldspar	54.7	624	85.72		−0.20	0.03	3		
	Illite	5.40	504	6.84		−0.10	0.02	3		
	Kaolinite	11.3								
TT-39-5	Bulk sample		321		10.50	−0.20	0.03	3		
	K-feldspar	24.0	563	42.06		−0.23	0.00	4		
	Chlorite	10.4	362	11.73		−0.30	0.03	4		
	Biotite	9.80	1160	35.40		−0.42	0.04	5		
	Plagioclase	32.4	2.39	0.24		0.01	0.06	5		
	Quartz	23.5	0.93	0.07						

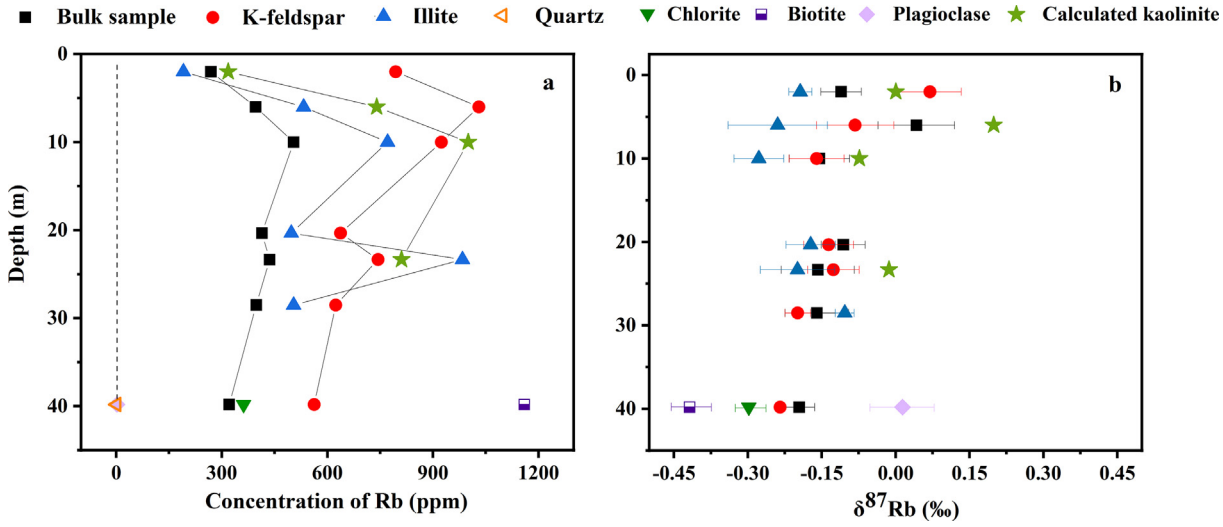

Fig. 4. The concentrations of Rb (a) and δ^{87}Rb (b) in different minerals during chemical weathering. The green stars represent the calculated Rb content and δ^{87}Rb of kaolinite, while other points represent the measured data. The vertical dashed line represents the assumed Rb concentrations of quartz and plagioclase in other samples.

Table 4
Rb concentrations and isotope compositions of stream water samples near Fogang weathering profile.

Sample	Sampling time	Na (μg/g)	Ca (μg/g)	Rb (ng/g)	δ^{87}Rb (‰)	2SD	n
LDR-20140917	09/17/2014	4.66	4.66	18.9	−0.22	0.04	3
LDR-20141117	11/17/2014	6.11	3.95	15.6	−0.40	0.03	4
LDR-20150117	01/17/2015	5.14	4.45	10.3	−0.17	0.02	3
LDR-20150316	03/16/2015	6.08	5.60	11.1	−0.19	0.02	3
LDR-20150518	05/18/2015	3.91	3.97	13.7	−0.19	0.08	4
LDR-20150727	07/27/2015	4.42	3.69	12.0	−0.10	0.08	4

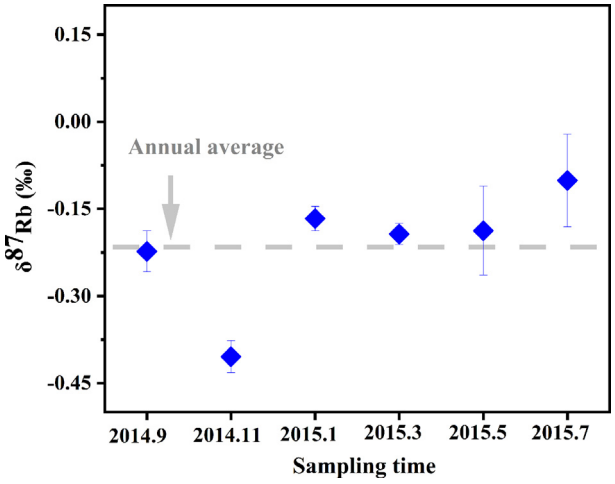

Fig. 5. The δ^{87}Rb value of stream water samples near the weathering profile with sampling time.

5.2.3. Rb isotopic composition of individual minerals in weathered residues

With the increase of weathering, biotite and chlorite disappear at approximately 31.6 m, and plagioclase at approximately 27.3 m. Above 29.5 m, the Rb concentration and isotopes budgets are mainly in K-feldspar, illite and kaolinite, as discussed below.

5.2.3.1. K-feldspar. K-feldspar is a primary mineral. The process of decomposition of K-feldspar can be expressed as the following reactions (Edmunds and Smedley, 2000; Teng et al., 2020):

$$3KAlSi_3O_8(\text{K-feldspar}) + 2H^+ + 12H_2O \rightarrow KAl_3Si_3O_{10}(OH)_2(\text{illite}) + 2K^+ + 6H_4SiO_4 \quad (5)$$

$$2KAl_3Si_3O_{10}(OH)_2(\text{illite}) + 2H^+ + 3H_2O \rightarrow 3Al_2Si_2O_5(OH)_4(\text{kaolinite}) + 2K^+ \quad (6)$$

The Rb^+ ions share the same site with K^+ in K-feldspar (Taylor, 1965; Shaw, 1968; Huntley and Hancock, 2001). During the decomposition of K-feldspar into illite and kaolinite, K^+ and Rb^+ will be gradually released (Schroeder, 1978). However, the Rb content of K-feldspar from Fogang profile increases from 624 μg/g in TT-28-3 to 1031 μg/g in TT-6, then decreases from TT-6 to 794 μg/g of TT-2. All these values are higher than Rb content of K-feldspar from parental rock (563 μg/g), indicating a process raising Rb content during K-feldspar decomposition. In addition, the Rb content variation of K-feldspar is

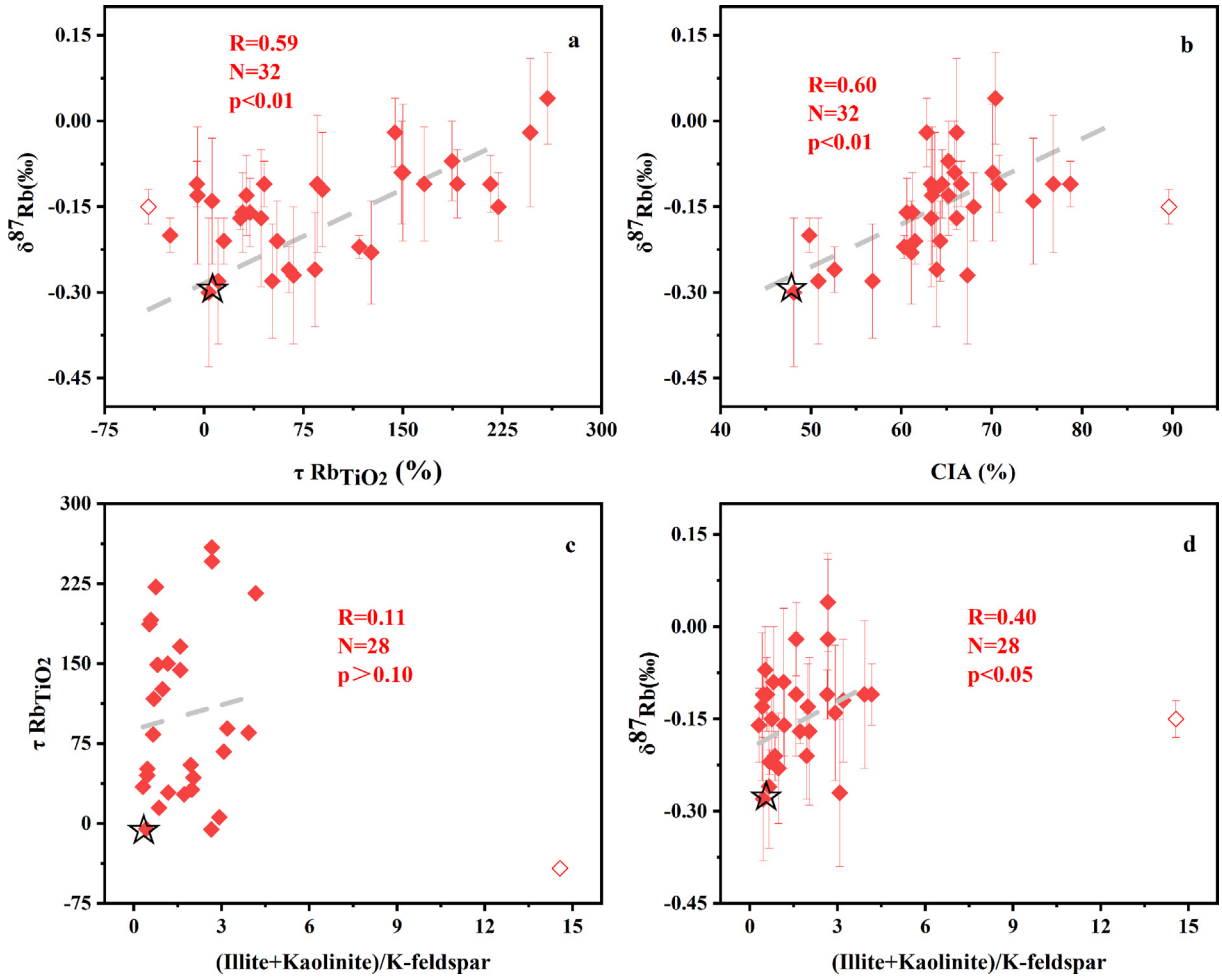

Fig. 6. Correlation between (a) τRb_{TiO_2} and $\delta^{87}Rb$; (b) CIA and $\delta^{87}Rb$; (c) (Illite + Kaolinite)/K-feldspar and τRb_{TiO_2} and (d) (Illite + Kaolinite)/K-feldspar and $\delta^{87}Rb$. The hollow star and diamond represent parent rock and TT-1, respectively. Sample TT-1 shows significant difference with other samples, which only contains 4.2 wt. % of K-feldspar but 61.2 wt. % of clay minerals. We deem that TT-1 may be influenced by topsoil, so the single datum was presented as hollowed-out diamond and not discussed with other data.

co-variant with τRb_{TiO_2} value of bulk sample (Fig. 2 and Fig. 4a). τRb_{TiO_2} value is a proxy to evaluate the relative depletion or enrichment of Rb during chemical weathering, which, together with total clay mineral (the sum of illite and kaolinite), revealing two processes in Fogang profile: (1) From 28.5 m to 6 m, τRb_{TiO_2} values considerably increase from 30% to 260%, accompanying the total clay mineral increase from 17 wt. % to 53 wt. %. The positive correlation between τRb_{TiO_2} and total clay mineral (Fig. 8a) imply that Rb^+ does not migrate out of the profile directly with the decomposition of primary minerals but is adsorbed by clay minerals again (Nesbitt et al., 1980). Rb has a lower hydration energy, which allows it to be easily absorbed by clay minerals, and even replace elements such as Mg^{2+} and K^+ in minerals (Teppen and Miller, 2006; Huang et al., 2012). (2) From 6 m to top, τRb_{TiO_2} value decreases from 55% to −42%. A strong negative correlation with the total clay mineral (from 43 wt. % ~ 61 wt. %) is observed (Fig. 8a), suggesting that this section underwent Rb desorption. The adsorption or desorption process of Rb can easily be influenced by pH value (Nesbitt et al., 1980; Sverjensky, 2006; Babechuk et al., 2014; Abedini and Khosravi, 2020). Acid environment causes alkalis adhered to the weathering products being replaced by H^+ and dissolved into water (Nesbitt et al., 1980; Babechuk et al., 2014). This explains the values of τRb_{TiO_2} decreasing from 259% to −42% from 6 m to the top of the weathering profile, where low pH values range from 4.88 to 5.42 are exhibited (Table 1 and Fig. 2), resulting in desorption of Rb^+. However, the pH values slowly rise to 7.03 from 6 m to 28.5 m, resulting in the leached Rb^+ or Rb^+ from decomposition attaching to clay minerals again (Fig. 2) (Nesbitt et al., 1980).

Given the facts that (1) K-feldspar has very limited adsorption ability of Rb compared to clay minerals, (2) Rb content of K-feldspar in weathered section is obviously higher than that in fresh rock (Fig. 4), and (3) Rb content of K-feldspar shows the similar variation with τRb_{TiO_2} value of the bulk rock that exhibit positive correlation with total clay mineral, we infer that Rb content variation of K-feldspar is related to the clay minerals attached on the corroded surface of K-feldspar (Bath

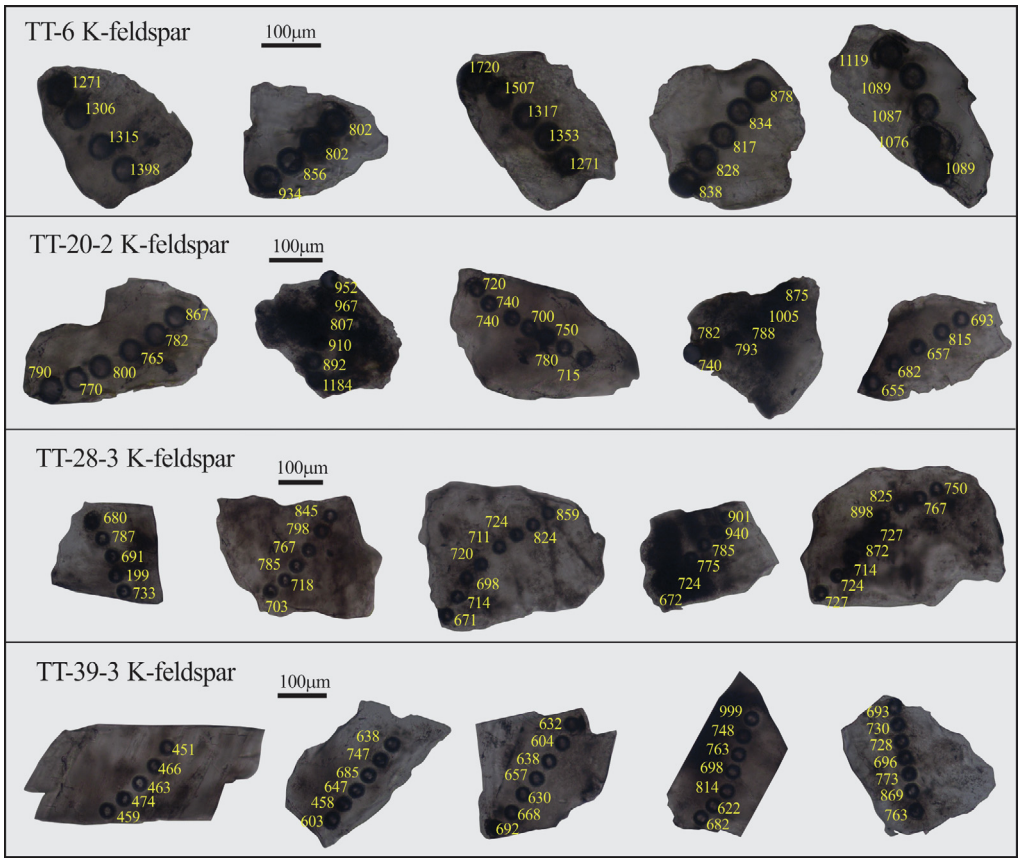

Fig. 7. The photomicrographs of K-feldspar grains from TT-6, TT-20-2, TT-28-3 and TT-39-3 under different weathering degree. The yellow number denotes the Rb concentration in μg/g of the in-situ analyses.

Table 5
Rb concentrations and isotope compositions of two portions of a certain mineral.

Sample	Mineral	Rb (μg/g)	δ^{87}Rb (‰)	2SD	n
TT-10	K-feldspar (1)	924	−0.15	0.04	5
	K-feldspar (2)	901	−0.18	0.05	3
TT-35-5	K-feldspar (1)	646	−0.09	0.10	5
	K-feldspar (2)	655	−0.16	0.06	3
TT-39-3	Biotite (1)	1310	−0.39	0.05	3
	Biotite (2)	1256	−0.40	0.04	3
TT-39-3	Plagioclase (1)	1.34	−0.02	0.04	3
	Plagioclase (2)	1.56	−0.03	0.01	2

et al., 1987). This is supported by the photomicrographs of K-feldspar crystals, showing the evolution from clean and euhedral grains to blurred and xenomorphic with the increase of weathering intensity (Fig. 7).

Rb isotopes are fractionated in K-feldspar from different depths. The δ^{87}Rb of K-feldspar varies from −0.23‰ in parent rock (TT-39-5) to 0.14‰ in TT-2 (Fig. 4b). Within 28.5 m to 6 m, the δ^{87}Rb values of K-feldspar (-0.20‰ in TT-28-3 to −0.13‰ in TT-10) only show < 0.10‰ fractionation compared with K-feldspar in parent rock ($\delta^{87}Rb_{\text{TT-39-5K-feldspar}}$ = -0.23‰). Larger isotope fractionation of K-feldspar is observed within 6 m of the surface (-0.08‰ in TT-6 and 0.14‰ in TT-2), where Rb content in K-feldspar increases along with total clay mineral. The variation may be caused by: (1) incongruent weathering of K-feldspar; (2) adsorption or desorption process influenced by clay minerals in altered K-feldspar. Given that the strong positive correlation between δ^{87}Rb of K-feldspar and the total clay mineral (Fig. 8b), the observed Rb isotope fractionation among K-feldspar in Fogang profile is more likely controlled by adsorption or desorption process of clay minerals which adhere on K-feldspar.

5.2.3.2. Illite. Illite is one of major clay minerals in Fogang weathering profile. Alkali metal elements, especially Rb and Cs can be easily adsorbed to illite via outer sphere adsorption to mineral surfaces (Pauley, 1953; Teppen and Miller, 2006), edge adsorption or intercalation into structural sites (Kim et al., 1996; Wampler et al., 2012; Fuller et al., 2015; Zaunbrecher et al., 2015) during chemical weathering. Rb contents of illite are basically above 500 μg/g in adsorption process, where the δ^{87}Rb values of illite display a decreasing trend from −0.10‰ in TT-28-3 to −0.24‰ in TT-6 (28.5 m – 6 m). In desorption process (6 m – 0 m), Rb contents of illite decrease from 532 μg/g of TT-6 to 191 μg/g of TT-2, and δ^{87}Rb values show an increasing trend from −0.24‰ in TT-6 to −0.19‰ in TT-2 (Fig. 4). The δ^{87}Rb values show

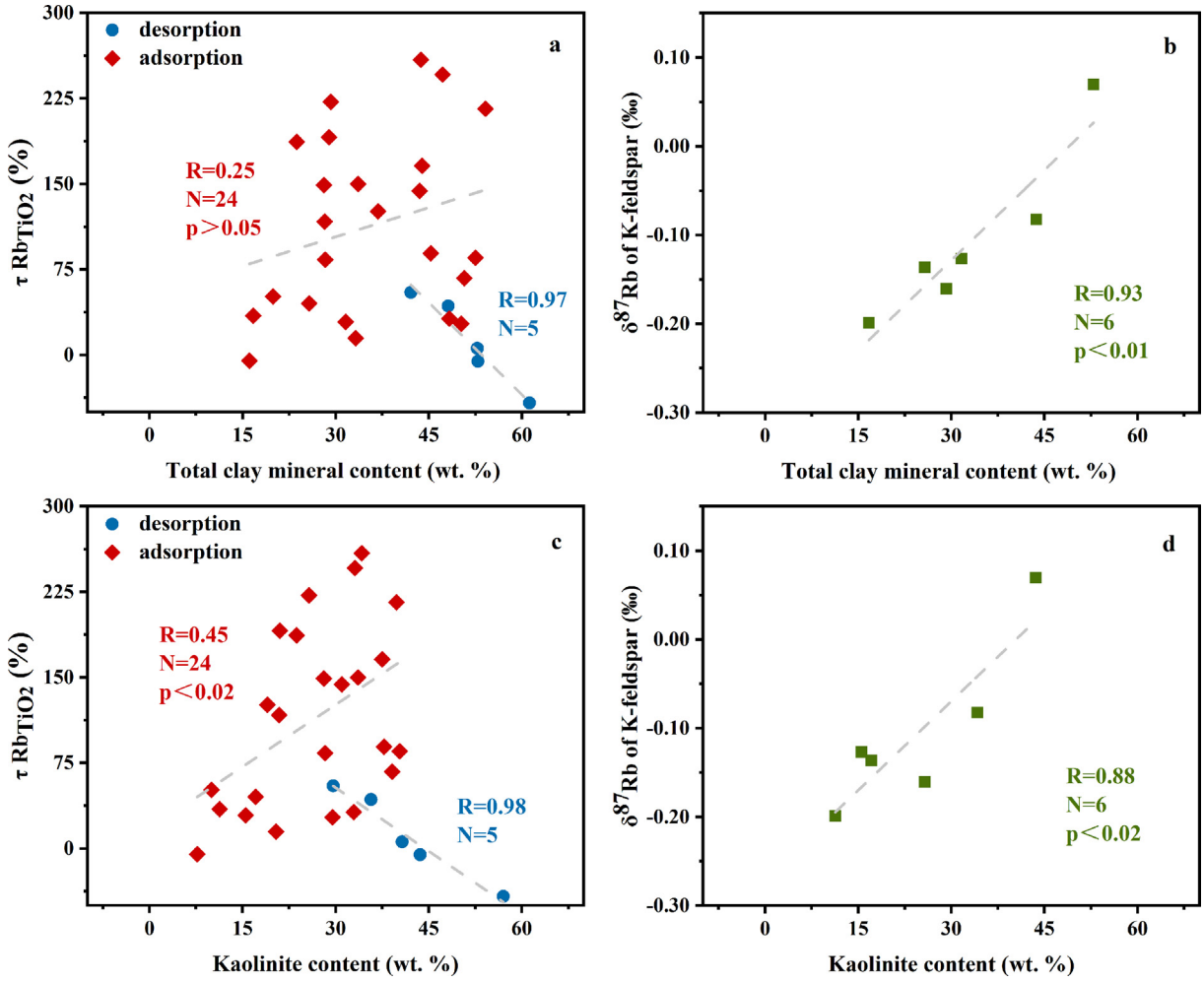

Fig. 8. Correlation of the total clay mineral (sum of illite and kaolinite proportion in wt. %) with (a) τRb_{TiO_2}, and with (b) the $\delta^{87}Rb$ value of K-feldspar; as well as correlation of the kaolinite content with (a) τRb_{TiO_2} and (b) the $\delta^{87}Rb$ value of K-feldspar. Red and blue dots denote the samples underwent adsorption process and desorption process, respectively.

that the fractionation among illite is about 0.18‰ in Fogang profile.

Illite is an intermediate product of decomposition of K-feldspar (equation 5 and 6), or biotite (equation 7 and 8) (Fordham, 1990; Bétard et al., 2009) to kaolinite. The latter reactions can be expressed as follows:

$$3\ K(MgFe)_3AlSi_3O_{10}(OH)_2(\text{biotite}) + 20H^+ \rightarrow KAl_3Si_3O_{10}(OH)_2(\text{illite}) + 2\,K^+ + 9(MgFe)^{2+} + 6H_4SiO_4 \quad (7)$$

$$2KAl_3Si_3O_{10}(OH)_2(\text{illite}) + 2H^+ + 3H_2O \rightarrow 3Al_2Si_2O_5(OH)_4(\text{kaolinite}) + 2\,K^+ \quad (8)$$

Both processes are likely to occur in Fogang profile, causing the Rb content and $\delta^{87}Rb$ value of illite to be influenced by the Rb released from the decomposition of the two primary minerals. Rb content of illite varies from 984 μg/g in TT-23-2 to 191 μg/g in TT-2 and shows the similar fluctuation as that of K-feldspar (Fig. 4a), suggesting that Rb adsorbed by illite may come from K-feldspar decomposition. However, the Rb content of illite in TT-23-2 reaches 984 μg/g, which is likely to be dominated by biotite decomposition as biotite has the highest Rb mineral (1160 μg/g) in the profile. The $\delta^{87}Rb$ values of illite are heavier than that of biotite in parent rock ($\delta^{87}Rb_{\text{TT-39-5biotite}} = -0.42‰$) but generally lighter than that of K-feldspar from the same depth, which may also be controlled by adsorption of Rb released from the decomposition of both biotite and K-feldspar.

5.2.3.3. Kaolinite. Kaolinite is the final product of chemical weathering in Fogang profile. Alkalis can be adsorbed to crystallite basal surfaces, edge sites, expandable layers, or by the cluster structure of kaolinite (Kim et al., 1996; Tian et al., 2015; Zhang et al., 2021a), which may result in Rb content variation and isotope fractionation.

The content of kaolinite increases gradually from 7.7 wt. % at 29.5 m to 57 wt. % at the top with the weathering intensity (Table 2). Limited by its size and morphology, kaolinite cannot be separated from the bulk samples, nor

can the Rb concentration and isotopic composition be measured. The influence of unselected kaolinite on Rb content and δ^{87}Rb for TT-39-5, TT-28-3 and TT-20-2 should be limited, because the sum of Rb content in available individual minerals account for more than 90%. However, Rb budget in available individual minerals from TT-23-2, TT-10, TT-6 and TT-2 is less than 75%, indicating that the unpicked kaolinite, the only possible host for this amount of Rb, cannot be neglected. Therefore, we roughly calculate the Rb content and isotopic composition of kaolinite by mass balance for furthering discussion. What should be mentioned is that the Rb content and δ^{87}Rb value of K-feldspar from parent rock (TT-39-5) is used for the calculation, to exclude the effect from clay minerals which influence the Rb content and δ^{87}Rb of K-feldspar under highly weathered environment as discussed above. The calculated Rb content of kaolinite varies from 318 μg/g to 1000 μg/g and the δ^{87}Rb values range from −0.07‰ to 0.20‰ (Fig. 4 and Table 3).

Similar to illite, kaolinite undergoes adsorption and desorption processes as well. Form 28.5 m to 6 m, τRb_{TiO_2} increases with the kaolinite proportion (Fig. 8c), suggesting that large amount of Rb is adsorbed into kaolinite. This is accompanied by increasing Rb content and δ^{87}Rb of kaolinite from TT-23-2 to TT-10 with the increase of weathering intensity. From 6 m to the surface of Fogang profile, τRb_{TiO_2} decreases with the continued increase of kaolinite proportion (Fig. 8c), indicating that kaolinite experienced a desorption process. The calculated Rb content of kaolinite gradually decreases, and δ^{87}Rb becomes lighter.

Overall, the δ^{87}Rb values of illite are heavier than biotite but lighter than K-feldspar, whereas kaolinite has the heaviest Rb isotopic composition in Fogang profile. In addition, the kaolinite content shows a good correlation with the δ^{87}Rb of K-feldspar but illite content does not (Fig. 8d). Therefore, the heavy Rb isotopic composition of altered K-feldspar and the whole weathered section is dominated by kaolinite. The Rb isotopes of 28.5 m to 6 m profile are controlled by clay minerals (mainly kaolinite) preferentially adsorbing the heavier Rb isotope, whereas the slight drop of δ^{87}Rb in the 6 m to top profile is controlled by desorption of Rb from clay minerals.

5.3. Implications for Rb isotope fractionation during chemical weathering

Granite is an important reservoir of Rb; therefore, the process of granite weathering has huge impact on transforming the δ^{87}Rb of river water and seawater over the Earth's history. Large Rb isotope fractionation occurring during chemical weathering is demonstrated by this study, with the heavy Rb isotope remaining in the weathered residues. This is further supported by the overall lighter δ^{87}Rb (except for the 20150727 sample that has a higher Rb isotopic composition of −0.10‰) of six nearby stream water samples (mean: -0.22 ± 0.10‰) compared to the saprolites near the profile surface, which are primarily fed by water from the surrounding mountains, suggesting that heavy Rb isotope preferred to be partitioned into weathered saprolites relative to fluids. Given that the δ^{87}Rb of bulk samples show good correlations with the CIA and τRb_{TiO_2} value (Fig. 6b), Rb isotopes could be a promising tracer for continental weathering, ocean chemistry and global Rb cycling.

Recent studies showed the great potential of isotopes of alkali elements (Li and K) in tracing chemical weathering (Teng et al., 2010; Misra and Froelich, 2012; Lechler et al., 2015; Santiago et al., 2018; Sun et al., 2018; Li et al., 2019; Chen et al., 2020; Teng et al., 2020). However, the wide range of δ^{7}Li in crustal materials hinders this proxy in reconstructing continent chemical weathering. Rb and K isotopes have some advantages in serving as such proxy, because they have a narrow range of isotopic compositions among most igneous rocks (Pringle et al., 2017; Zhang et al., 2018; Li et al., 2019) but the isotope fractionation in weathering is large.

However, Rb and K do not always behave in the same way (Nesbitt et al., 1980). The K/Rb ratio (g/g) in Earth's inner reservoirs varies slightly (400 for the BSE and 232 for crust) (Shaw, 1968; Rudnick and Gao, 2014), but the ratio in hydrosphere varies significantly (1000 in rivers and 3765 in seawater) (Fabricand et al., 1966; Peltola et al., 2008). Chemical weathering plays a crucial role in modifying the K/Rb ratio. This is confirmed by τRb_{TiO_2} and τK_{TiO_2} which co-vary during the early weathering stage but are decoupled on the upper profile (Fig. 9). Rb shows a more significant enrichment trend than K in the upper weathering products. The processes in clay minerals may play pivotal role in changes of K/Rb ratio, because: (1) The alkali elements released by decomposition are easily adsorbed by clay minerals. Compared with K^+, Rb^+ has a relatively lower hydration energy, which allows Rb^+ to adhere more easily onto the surface of clay minerals than K^+ and be fixed more strongly, acting like an immobile element (Nesbitt et al., 1980; Teppen and Miller, 2006; Huang et al., 2012). (2) 2:1 sheet structure mineral such as illite and mica will form frayed edge wedges during chemical weathering. Rb^+ and Cs^+ from the soil solution can replace K^+ which is previously fixed in the interlayers (Zaunbrecher et al., 2015). It is probably these processes that reduce the K/Rb ratio in weathered residues and raise that of rivers and seawater. In addition, Rb and K isotopes behave differently as well. The K isotopic compositions of the bulk samples in the Fogang profile had been measured by Teng et al. (2020). In contrast to Rb isotopes, the K isotopic compositions in the whole profile change from −0.49‰ to −0.65‰ from the unaltered rock to the top, and δ^{41}K gradually becomes lighter with the enhancement of chemical weathering (Fig. 9). This is also confirmed by another study where a negative correlation between CIA values and δ^{41}K in river sediments is found (Li et al., 2019), which differs from the positive correlation between Rb isotopes and CIA in this study. The reverse trend may be influenced by the difference in coordination numbers and bond energy in clay minerals and soil solutions between Rb and K. In general, higher coordination number and lower bond energy prefer light isotope. The coordination number of both Rb and K in clay minerals is 8 (Zaunbrecher et al., 2015; Sposito et al., 1999). The coordination number of Rb in solutions ranges from

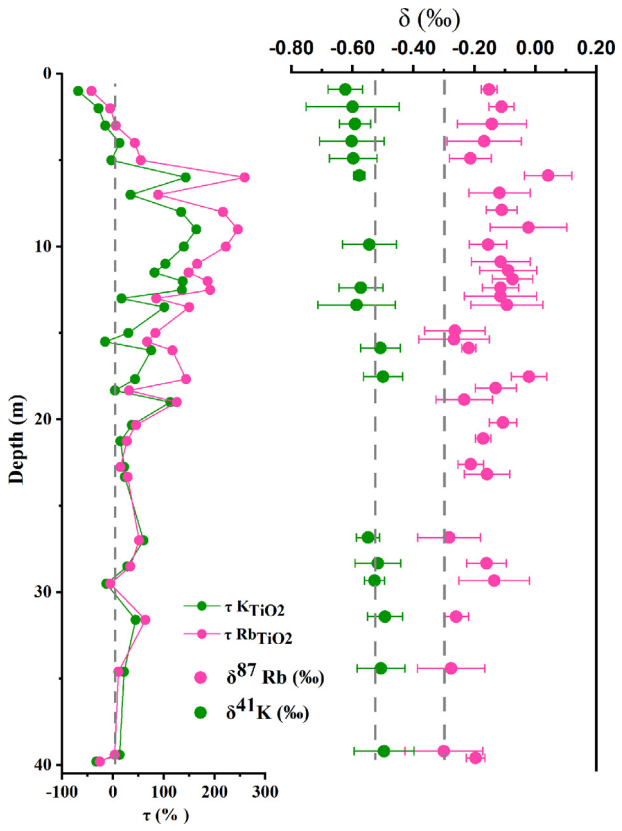

Fig. 9. The variations of τK_{TiO_2}, τRb_{TiO_2}, $\delta^{87}Rb$ and $\delta^{41}K$ with depth.

5.6 to 8.9 (Caralampio et al., 2017), whereas that of K varies from 4.0 to 8.3 (Smirnov and Trostin, 2007; Varma and Rempe, 2006). We hypothesized that the differences in Rb and K coordination numbers between the solution and the clay minerals lead to the opposite fractionation trend of the two isotopes. More work is needed to answer this question. Nevertheless, in-depth study on Rb isotope fractionation during chemical weathering may provide unique information that isotopes of other alkali elements cannot.

6. CONCLUSIONS

Rb mobility and isotopic ratios among the bulk samples and major host minerals from a 40 m-long granite chemical weathering profile in Guangdong Province, South China, and of surrounding stream water samples are investigated, to explore the mechanism triggering Rb isotope fractionation during chemical weathering. The main conclusions reached by this study are listed as follows:

1. The Rb isotopic compositions show significant fractionation along the whole profile, with $\delta^{87}Rb$ ranging from −0.30‰ in the unaltered granite to 0.04‰ in weathered saprolites.
2. The Rb isotopic compositions display an obvious correlation with the value of τRb_{TiO_2} and CIA, suggesting that chemical weathering drives ^{87}Rb to be enriched in the weathered residues.
3. Variations of $\delta^{87}Rb$ exist among different mineral species from the same bulk samples and the same mineral species from different depths. Kaolinite, the final product of chemical weathering, has the heaviest isotopic composition in Fogang profile.
4. The adsorption and desorption processes of kaolinite is the main reason for Rb concentration change and isotope fractionation in Fogang profile.
5. Stream water has lighter $\delta^{87}Rb$ value than the weathered saprolites in the upper part of the profile.

Declaration of Competing Interest

The authors declare that they have no known competing financial interests or personal relationships that could have appeared to influence the work reported in this paper.

ACKNOWLEDGEMENTS

The authors would like to thank Dr. Xianglin Tu and Dr. Shengling Sun of the State Key Laboratory of Isotope Geochemistry, GIG-CAS, for their assistance with Thermo Element ICP-MS measurements. We also thank Prof. Fangzhen Teng, Prof. Jianxi Zhu, Chutian Shu, and Shangying Li for their constructive suggestions. The English of the manuscript was polished by American Journal Experts. This work was supported by grants from the National Natural Science Foundation of China (Grants 41991325, 41573003 and 42021002), the Fundamental and Applied Fundamental Research Major Program of Guangdong Province (2019B030302013), the Key Special Project for Introduced Talents Team of Southern Marine Science and Engineering Guangdong Laboratory (Guangzhou) (GML2019ZD0308), and the GIGCAS 135 project (Grant 135PY201605). This paper is contribution No. IS-3059 from the GIG-CAS.

APPENDIX A. SUPPLEMENTARY MATERIAL

Supplementary data to this article can be found online at https://doi.org/10.1016/j.gca.2021.08.010.

REFERENCES

Abedini A. and Khosravi M. (2020) Geochemical constraints on the Triassic-Jurassic Amir-Abad karst-type bauxite deposit NW Iran. *J. Geochem. Explor.* **211** 106489.

Babechuk M. G., Widdowson M. and Kamber B. S. (2014) Quantifying chemical weathering intensity and trace element release from two contrasting basalt profiles, Deccan Traps, India. *Chem. Geol.* **363**, 56–75.

Bath A. H., Milodowski A. E. and Strong G. E. (1987) Fluid flow and diagenesis in the East Midlands Triassic sandstone aquifer. *Spec. Publ. Geological Society* **34**, 127–140.

Beattie P., Drake M., Johns J., Leeman W., Longhi J., Mckay G., Nielsen R., Palme H., Shaw D., Takahashi E. and Watson B. (1993) Terminology for trace-element partitioning. *Geochim. Cosmochim. Acta* **57**, 1605–1606.

Berg T., Royset O. and Steinnes E. (1994) Trace-elements in atmospheric precipitation at Norwegian background stations (1989–1990) measured by ICP-MS. *Atmos. Environ.* **28**, 3519–3536.

Berner E. K. and Berner R. A. (2012) *Global Environment: Water*. Princeton University Publisher, Air and Geochemical Cycles, p. 488.

Bétard F., Caner L., Gunnell Y. and Bourgeon G. (2009) Illite neoformation in plagioclase during weathering: evidence from semi-arid Northeast Brazil. *Geoderma* **152**, 53–62.

Calmels D., Gaillardet J. and François L. (2014) Sensitivity of carbonate weathering to soil CO_2 production by biological activity along a temperate climate transect. *Chem. Geol.* **390**, 74–86.

Caralampio D. Z., Martínez J. M., Pappalardo R. R. and Marcos E. S. (2017) The hydration structure of the heavy-alkalines Rb^+ and Cs^+ through molecular dynamics and X-ray absorption spectroscopy: surface clusters and eccentricity. *Phys. Chem. Chem. Phys.* **19**, 28993–29004.

Carey A. E., Lyons W. B. and Owen J. S. (2005) Significance of landscape age, uplift, and weathering rates to ecosystem development. *Aquatic Geochem.* **11**, 215–239.

Chen H., Liu X. M. and Wang K. (2020) Potassium isotope fractionation during chemical weathering of basalts. *Earth Planet. Sci. Lett.* **539** 116192.

Cui L. F., Liu C. Q., Xu S., Zhao Z. Q., Liu T. Z., Liu W. J. and Zhang Z. J. (2016) Subtropical denudation rates of granitic regolith along a hill ridge in Longnan, SE China derived from cosmogenic nuclide depth-profiles. *J. Asian Earth Sci.* **117**, 146–152.

Cui L., Liu C., Xu S., Zhao Z., Tu C., Liu T. and Ding H. (2014) The long-term denudation rate of granitic regolith in Qinhuangdao, North China determined from the in situ depth profile of the cosmogenic nuclides ^{26}Al and ^{10}Be. *Chin. Sci. Bull.* **59**, 4823–4828.

Dessert C., Dupré B., Gaillardet J., François L. M. and Allègre C. J. (2003) Basalt weathering laws and the impact of basalt weathering on the global carbon cycle. *Chem. Geol.* **202**, 257–273.

Edmunds W. M. and Smedley P. L. (2000) Residence time indicators in groundwater: the East Midlands Triassic sandstone aquifer. *Appl. Geochem.* **15**, 737–752.

Fabricand B. P., Imbimbo E. S., Brey M. E. and Weston J. A. (1966) Atomic absorption analyses for Li, Mg, K, Rb, and Sr in ocean waters. *J. Geophys. Res.* **71**, 3917–3921.

Fordham A. W. (1990) Formation of Trioctahedral Illite from biotite in a soil profile over granite gneiss. *Clays Clay Miner.* **38**, 187–195.

Fuller A. J., Shaw S., Ward M. B., Haigh S. J., Mosselmans J. F. W., Peacock C. L., Stackhouse S., Dent A. J., Trivedi D. and Burke I. T. (2015) Caesium incorporation and retention in illite interlayers. *Appl. Clay Sci.* **108**, 128–134.

Gaillardet J., Dupré B., Louvat P. and Allègre C. J. (1999) Global silicate weathering and CO_2 consumption rates deduced from the chemistry of large rivers. *Chem. Geol.* **159**, 3–30.

Huang K. J., Teng F. Z., Wei G. J., Ma J. L. and Bao Z. Y. (2012) Adsorption-and desorption-controlled magnesium isotope fractionation during extreme weathering of basalt in Hainan Island, China. *Earth Planet. Sci. Lett.* **359–360**, 73–83.

Huntley D. J. and Hancock R. G. V. (2001) The Rb contents of the K-feldspar grains being measured in optical dating. *Ancient TL* **19**, 43–46.

Kim Y., Cygan R. T. and Kirkpatrick R. J. (1996) ^{133}Cs NMR and XPS investigation of cesium adsorbed on clay minerals and related phases. *Geochim. Cosmochim. Acta.* **60**, 1041–1052.

Kuhlemann J., Borg K. V. D., Bons P. D., Danišík M. and Frisch W. (2007) Erosion rates on subalpine paleosurfaces in the western Mediterranean by in-situ ^{10}Be concentrations in granites: implications for surface processes and long-term landscape evolution in Corsica (France). *Int. J. Earth Sci.* **97**, 549–564.

Lara M. C., Buss H. L., Pogge von Strandmann P. A. E., Dessert C. and Gaillardet J. (2014) Controls on the Mg cycle in the tropics: insights from a case study at the luquillo critical zone observatory. *Proc. Earth Planet. Sci.* **10**, 200–203.

Lechler M., Pogge von Strandmann P. A. E., Jenkyns H. C., Prosser G. and Parente M. (2015) Lithium-isotope evidence for enhanced silicate weathering during OAE 1a (Early Aptian Selli event). *Earth Planet. Sci. Lett.* **432**, 210–222.

Li S., Li W., Beard B. L., Raymo M. E., Wang X., Chen Y. and Chen J. (2019) K isotopes as a tracer for continental weathering and geological K cycling. *Proc. Natl. Acad. Sci. United States America* **116**, 8740–8745.

Li X., Li W., Wang X., Li Q., Liu Y. and Tang G. (2009) Role of mantle-derived magma in genesis of early Yanshanian granites in the Nanling Range, South China: in situ zircon Hf-O isotopic constraints. *Sci. China Ser. D Earth Sci.* **52**, 1262–1278.

Lodders K. (2003) Solar system abundances and condensation temperatures of the elements. *Astrophys. J.* **591**, 1220–1247.

Ma J., Wei G., Xu Y. and Long W. (2010) Variations of Sr–Nd–Hf isotopic systematics in basalt during intensive weathering. *Chem. Geol.* **269**, 376–385.

Mahara Y., Hohjo K., Kubota T., Ohta T., Mizuochi Y., Tashiro T., Sekimoto S., Takamiya K., Shibata S. and Tanaka K. (2010) Vertical distribution of ^{10}Be, ^{26}Al, and ^{36}Cl in the surface soil layer of weathered granite at Abukuma, Japan. *Nucl. Instrum. Methods Phys. Res., Sect. B: Beam Interact. Mater. Atoms* **268**, 1197–1200.

McDonough W. F. and Sun S. S. (1995) The composition of the Earth. *Chem. Geol.* **120**, 223–253.

Mckenzie D. and O'Nions R. K. (1991) Partial melt distributions from inversion of rare earth element concentrations. *J. Petrol.* **32**, 1021–1091.

Misra S. and Froelich P. N. (2012) Lithium isotope history of Cenozoic seawater: changes in silicate weathering and reverse weathering. *Science* **335**, 818–823.

Nebel O., Mezger K., Scherer E. E. and Münker C. (2005) High precision determinations of $^{87}Rb/^{85}Rb$ in geologic materials by MC-ICP-MS. *Int. J. Mass Spectrom.* **246**, 10–18.

Nebel O., Mezger K. and Westrenen W. V. (2011a) Rubidium isotopes in primitive chondrites: constraints on Earth's volatile element depletion and lead isotope evolution. *Earth Planet. Sci. Lett.* **305**, 309–316.

Nebel O., Scherer E. E. and Mezger K. (2011b) Evaluation of the ^{87}Rb decay constant by age comparison against the U-Pb system. *Earth Planet. Sci. Lett.* **301**, 1–8.

Nesbitt H. W. (1979) Mobility and fractionation of rare earth elements during weathering of a granodiorite. *Nature* **279**, 206–210.

Nesbitt H. W., Markovics G. and Price R. C. (1980) Chemical processes affecting alkalis and alkaline earths during continental weathering. *Geochim. Cosmochim. Acta* **44**, 1659–1666.

Nesbitt H. W. and Young G. M. (1982) Early Proterozoic climates and plate motions inferred from major element chemistry of lutites. *Nature* **299**, 715–717.

Nie N. X. and Dauphas N. (2019) Vapor drainage in the protolunar disk as the cause for the depletion in volatile elements of the moon. *Astrophys. J.* **884**, L48.

Opfergelt S. and Delmelle P. (2012) Silicon isotopes and continental weathering processes: assessing controls on Si transfer to the ocean. *Comptes Rendus Geosci.* **344**, 723–738.

Pauley J. L. (1953) Prediction of Cation-exchange Equilibria. *J. Am. Chem. Soc.* **76**, 1422–1425.

Peltola P., Brun C., Åström M. and Tomilina O. (2008) High K/Rb ratios in stream waters — exploring plant litter decay, ground water and lithology as potential controlling mechanisms. *Chem. Geol.* **257**, 92–100.

Pistiner J. S. and Henderson G. M. (2003) Lithium-isotope fractionation during continental weathering processes. *Earth Planet. Sci. Lett.* **214**, 327–339.

Pringle E. A. and Moynier F. (2017) Rubidium isotopic composition of the Earth, meteorites, and the Moon: evidence for the origin of volatile loss during planetary accretion. *Earth Planet. Sci. Lett.* **473**, 62–70.

Raymo M. E., Ruddiman W. F. and Froelich P. N. (1988) Influence of late Cenozoic mountain building on ocean geochemical cycles. *Geol.* **16**, 649.

Rudnick R. L. and Gao S. (2014) Composition of the Continental Crust. In *The Crust* (ed. R. L. Rudnick). Treatise on Geochemistry, Elsevier-Pergamon, Oxford, pp. 1–51.

Santiago Ramos D.P., Morgan L.E., Lloyd N.S., Higgins J.A., 2018. Reverse weathering in marine sediments and the geochemical cycle of potassium in seawater: Insights from the K isotopic composition (41K/39K) of deep-sea pore-fluids. Geochim. Cosmochim. Acta 236, 99–120.

Schroeder D. (1978) Structure and weathering of potassium containing minerals. *IPI Research Topics*, 5–25.

Shaw D. M. (1968) A review of K-Rb fractionation trends by covariance analysis. *Geochim. Cosmochim. Acta* **37**, 573–601.

Shimamura T., Iwashita M., Iijima S., Shintani M. and Takaku Y. (2007) Major to ultra trace elements in rainfall collected in suburban Tokyo. *Atmos. Environ.* **41**, 6999–7010.

Siebert C., Pett-Ridge J. C., Opfergelt S., Guicharnaud R. A., Halliday A. N. and Burton K. W. (2015) Molybdenum isotope fractionation in soils: Influence of redox conditions, organic matter, and atmospheric inputs. *Geochim. Cosmochim. Acta* **162**, 1–24.

Smirnov P. R. and Trostin V. N. (2007) Structures of the nearest surroundings of the K^+, Rb^+, and Cs^+ ions in aqueous solutions of their salts. *Russ. J. Gen. Chem.* **77**, 2101–2107.

Stössel R.-P. and Prange A. (1985) Determination of trace elements in rainwater by total-reflection x-ray fluorescence. *Anal. Chem.* **57**, 2880–2885.

Sun H., Xiao Y., Gao Y., Zhang G., Casey J. F. and Shen Y. (2018) Rapid enhancement of chemical weathering recorded by extremely light seawater lithium isotopes at the Permian-Triassic boundary. *Proc. Natl. Acad. Sci. United States America* **115**, 3782–3787.

Sverjensky D. A. (2006) Prediction of the speciation of alkaline earths adsorbed on mineral surfaces in salt solutions. *Geochim. Cosmochim. Acta* **70**, 2427–2453.

Taylor S. R. (1965) The application of trace element data to problems in petrology. *Phys. Chem. Earth* **6**, 133–213.

Taylor S. R., Mclennan S. M. and Mcculloch M. T. (1983) Geochemistry of loess, continental crustal composition and crustal model ages. *Geochim. Cosmochim. Acta* **47**, 1897–1905.

Teng F. Z., Li W. Y., Rudnick R. L. and Gardner L. R. (2010) Contrasting lithium and magnesium isotope fractionation during continental weathering. *Earth Planet. Sci. Lett.* **300**, 63–71.

Teng F. Z., Dauphas N. and Watkins J. M. (2017) Non-traditional stable isotopes: retrospective and prospective. *Rev. Mineral. Geochem.* **82**, 1–26.

Teng F. Z., Hu Y., Ma J. L., Wei G. J. and Rudnick R. L. (2020) Potassium isotope fractionation during continental weathering and implications for global K isotopic balance. *Geochim. Cosmochim. Acta* **278**, 261–271.

Teppen B. J. and Miller D. M. (2006) Hydration energy determines isovalent cation exchange selectivity by clay minerals. *Soil Sci. Soc. Am. J.* **70**, 31.

Tian R., Yang G., Tang Y., Liu X., Li R., Zhu H. and Li H. (2015) Origin of hofmeister effects for complex systems. *PLOS One* **10** e0128602.

Tsai P. H., You C. F., Huang K. F., Chung C. H. and Sun Y. B. (2014) Lithium distribution and isotopic fractionation during chemical weathering and soil formation in a loess profile. *J. Asian Earth Sci.* **87**, 1–10.

Varma S. and Rempe S. B. (2006) Coordination numbers of alkali metal ions in aqueous solutions. *Biophys. Chem.* **124**, 192–199.

Wampler J. M., Krogstad E. J., Elliott W. C., Kahn B. and Kaplan D. I. (2012) Long-term selective retention of natural Cs and Rb by highly weathered coastal plain soils. *Environ. Sci. Technol.* **46**, 3837–3843.

Wang Z., Ma J., Li J., Wei G., Zeng T., Li L., Zhang L., Deng W., Xie L. and Liu Z. (2018) Fe (hydro) oxide controls Mo isotope fractionation during the weathering of granite. *Geochim. Cosmochim. Acta* **226**, 1–17.

Wang Z., Ma J., Li J., Zeng T., Zhang Z., He X., Zhang L. and Wei G. (2020) Effect of Fe–Ti oxides on Mo isotopic variations in lateritic weathering profiles of basalt. *Geochim. Cosmochim. Acta* **286**, 380–403.

Wedepohl K. H. (1995) The composition of the continental crust. *Geochim. Cosmochim. Acta* **59**, 1217–1232.

You C.-F., Castillo P. R., Gieskes J. M., Chan L. H. and Spivack A. J. (1996) Trace element behavior in hydrothermal experiments: implications for fluid processes at shallow depths in subduction zones. *Earth Planet. Sci. Lett.* **140**, 41–52.

Zaunbrecher L. K., Cygan R. T. and Elliott W. C. (2015) Molecular models of cesium and rubidium adsorption on weathered micaceous minerals. *J. Phys. Chem. A* **119**, 5691–5700.

Zeng H., Rozsa V. F., Nie N. X., Zhang Z., Pham T. A., Galli G. and Dauphas N. (2019) Ab initio calculation of equilibrium isotopic fractionations of potassium and rubidium in minerals and water. *ACS Earth Space Chem.* **3**, 2601–2612.

Zhang L., Ren Z. Y., Xia X. P., Yang Q., Hong L. B. and Wu D. (2019) In situ determination of trace elements in melt inclusions using laser ablation inductively coupled plasma sector field mass spectrometry. *Rapid Commun. Mass Spectrom.* **33**, 361–370.

Zhang Z., Ma J., Zhang L., Liu Y. and Wei G. (2018) Rubidium purification via a single chemical column and its isotope measurement on geological standard materials by MC-ICP-MS. *J. Anal. At. Spectrom.* **33**, 322–328.

Zhang Z., Zhou Q., Yuan Z., Zhao L. and Dong J. (2021a) Adsorption of Mg^{2+} and K^+ on the kaolinite (0 0 1) surface in aqueous system: a combined DFT and AIMD study with an experimental verification. *Appl. Surf. Sci.* **538** 148158.

Zhang Z. J., Nie N. X., Mendybaev R. A., Liu M.-C., Hu J. J., Hopp T., Alp E. E., Lavina B., Bullock E. S., McKeegan K. D. and Dauphas N. (2021b) Loss and isotopic fractionation of alkali elements during diffusion-limited evaporation from molten silicate: theory and experiments. *ACS Earth Space Chem.* **5**, 755–784.

Associate editor: Brian W. Stewart